Dynamics in a two-dimensional core-softened fluid

Philip J. Camp*
School of Chemistry, University of Edinburgh, West Mains Road, Edinburgh EH9 3JJ, United Kingdom
(Received 27 July 2004; revised manuscript received 27 December 2004; published 25 March 2005)

The dynamical properties of a model one-component core-softened fluid with purely repulsive interactions are found to be very complex. At low temperature the fluid structure exhibits cluster motifs including dimers, stripes, and polygons, depending on density. Single-particle diffusion and the velocity, shear-stress, and wave-vector-dependent current correlation functions have all been calculated using molecular dynamics simulations. The results highlight the presence of well-resolved single-particle and collective motions, which is remarkable for what is essentially a "simple" one-component fluid.

DOI: 10.1103/PhysRevE.71.031507 PACS number(s): 61.20.Lc, 62.60.+v, 68.08.De

I. INTRODUCTION

The intermolecular potential in a core-softened fluid (CSF) consists of a hard repulsive core and a "soft" repulsive shoulder, and sometimes an attractive tail. CSFs have received considerable attention as models with which to understand the origins of unusual phenomena—such as negative thermal expansion and liquid-liquid critical points—in network-forming systems such as water [1], liquid phosphorus [2], and liquid carbon [3]. These materials are characterized by the ability of the constituent particles to form two (or more) types of "bond" with nearest neighbors; the CSF mimics this effect through pairs of particles either penetrating, or being repulsed by, the shoulder of the potential. To date the study of model CSFs has been restricted to static structural and thermodynamic properties [4–14].

In recent work the structure and phase behavior of an interesting model two-dimensional CSF were studied using Monte Carlo (MC) computer simulations [13]. The model consists of a monolayer of Lennard-Jones spheres with an additional long-range repulsive interaction. The pair interaction potential is

$$u(r) = 4\epsilon\left[\left(\frac{\sigma}{r}\right)^{12} - \left(\frac{\sigma}{r}\right)^{6}\right] + \epsilon'\left(\frac{\sigma}{r}\right)^{3}, \qquad (1)$$

where ϵ and ϵ' are energy parameters, σ is the sphere "diameter," and r is the interparticle separation. A physical realization of this model might be a monolayer of ferromagnetic surface-stabilized colloidal particles on a solid substrate, with a strong magnetic field aligned perpendicular to the plane. With the energy parameter $\epsilon' = (8\sqrt{6}/9)\epsilon$, $u(r)$ is purely repulsive and consists of a short-range repulsive core, a shoulder of height $\epsilon/3$ at $r \simeq 1.35\sigma$, and a slowly decaying repulsive tail; the potential function is plotted in Fig. 1(a). Results from MC simulations show that at low reduced temperatures $T^* \equiv k_B T/\epsilon \sim 10^{-2}$ (k_B is Boltzmann's constant) this pair potential gives rise to an astonishing range of states including dimerized, striped, and meshlike fluids, and triangular and Kagomé lattices [13]. Some typical fluid configurations obtained from MC simulations are shown in Fig. 1 (see Sec. III for discussion). A similar diversity of structures has been observed in a two-dimensional model consisting of hard disks with a repulsive "step" potential [12].

The objective of the current work is to survey the dynamical properties of the CSF at a level of detail comparable to that obtained in simulation studies of simple "atomic" fluids [15,16]; the plan of attack has been inspired by recent simulation studies of dynamics in complex fluids and glasses, such as amorphous silica (see, e.g., Ref. [17]). To this end, molecular dynamics (MD) simulations have been used to calculate various dynamical features, including single-particle diffusion, relaxation of shear-stress correlations, and longitudinal and transverse current correlations. It is observed that at moderate densities the structures evident in Fig. 1 give rise to motions with two distinct time scales: high-frequency motions corresponding to single-particle movement within clusters and low-frequency motions corresponding to fluctuations in the cluster network. The main conclusion from this work is that the model two-dimensional CSF under consideration not only possesses unusually rich phase behavior, and unusual structural motifs, but also plays host to complex dynamical phenomena. This is particularly interesting because the model is ostensibly a "simple" one-component fluid with purely repulsive interactions.

This paper is organized as follows. In Sec. II the simulation methods are summarized briefly. Simulation results are presented in Sec. III, which begins with a recap of the key structural features, and then goes on to report single-particle and collective dynamical properties in turn. Section IV concludes the paper.

II. MOLECULAR DYNAMICS SIMULATIONS

The dynamical properties of the CSF defined in Eq. (1) with $\epsilon' = (8\sqrt{6}/9)\epsilon$ were examined using molecular dynamics (MD) simulations in the Gaussian isokinetic ensemble [18]. The system consisted of $N = 500$ particles in a square simulation cell of area $A = L^2$, with periodic boundary conditions applied. The dimensionless parameters in the system include number density $\rho^* = N\sigma^2/A$, temperature $T^* = k_B T/\epsilon$, and time $t^* = t\sqrt{\epsilon/m\sigma^2}$. The potential was truncated smoothly between $0.95 \times L/2$ and $L/2$ using the switching function of Ref. [19]. The equations of motion were integrated over 10^6 time steps of length $\delta t^* = 0.005$ using the fourth-order Gear predictor-corrector algorithm [18]. Time correlation func-

*Email address: philip.camp@ed.ac.uk

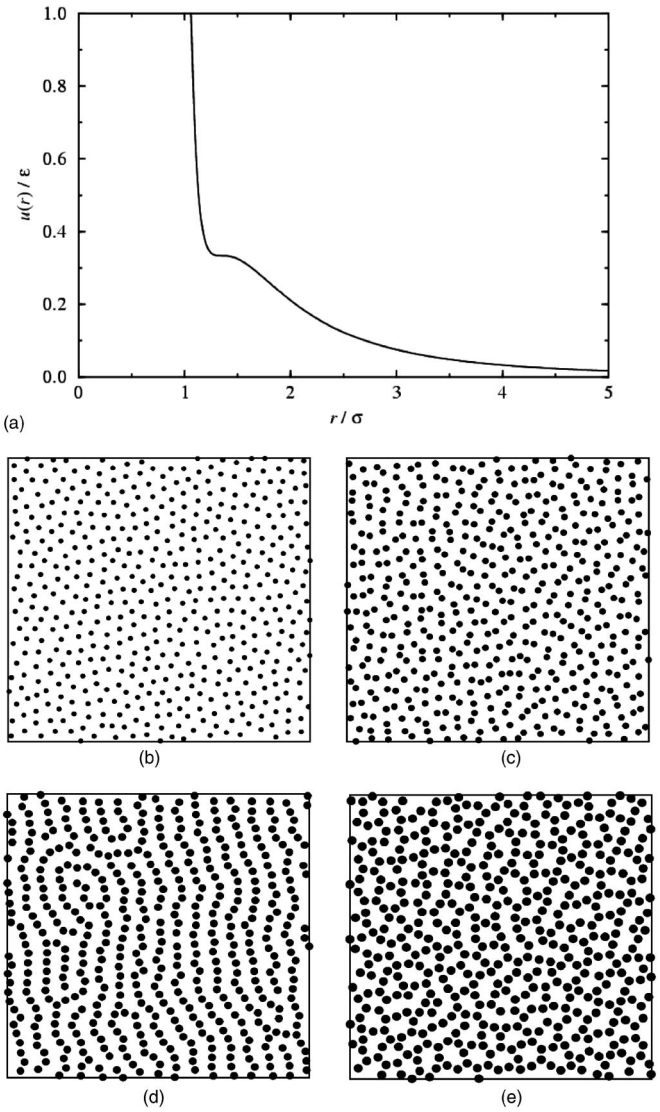

FIG. 1. (a) Pair interaction potential, $u(r)$ [Eq. (1)] with $\epsilon' = (8\sqrt{6}/9)\epsilon$. (b)–(e) Snapshots from simulations of the CSF at $T^* = 0.01$ and various densities: (b) $\rho^* = 0.15$, (c) $\rho^* = 0.25$, (d) $\rho^* = 0.35$, and (e) $\rho^* = 0.45$. Spheres are shown with diameter 1σ.

tions in the time interval $0 \leqslant t^* \leqslant 100$ were measured and averaged over 50 blocks, each consisting of 20,000 time steps.

III. RESULTS

Results are reported for the CSF at reduced densities in the range $0.05 \leqslant \rho^* \leqslant 0.45$ along a single isotherm with reduced temperature $T^* = 0.01$, for which there is only one manifold of stable solid phases at high densities $\rho^* \gtrsim 0.5$ [13]. Before proceeding with an account of the dynamical properties of the CSF, the relevant structural characteristics will be summarized. Figure 1 shows simulation snapshots of the CSF at densities $\rho^* = 0.15$, 0.25, 0.35, and 0.45. The progression of structures from "normal," to striped-liquid, and then to meshlike structures is remarkable. Spatial correlation functions and cluster distributions are discussed fully in Ref. 13, but the images in Fig. 1 will be sufficient for interpreting what follows.

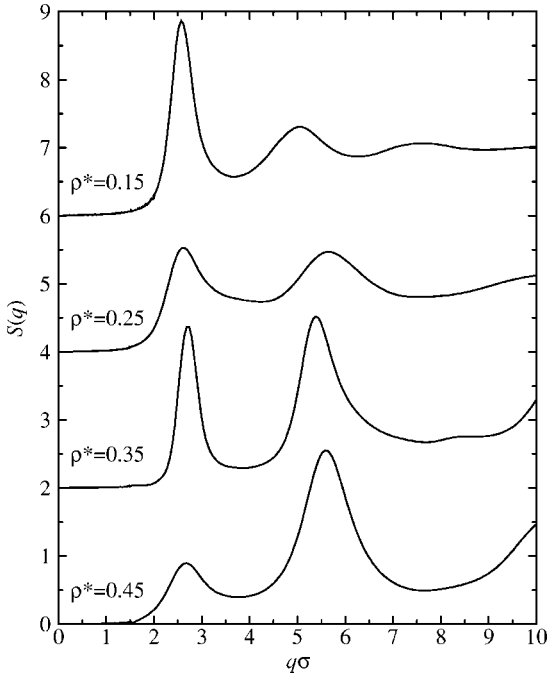

FIG. 2. Structure factor, $S(q)$, in the CSF at $T^* = 0.01$ and densities (from top to bottom) $\rho^* = 0.15$, 0.25, 0.35, and 0.45. The curves are displaced by two units along the ordinate for clarity.

To identify the characteristic structural length scales present in the CSF, consider the static structure factor,

$$S(q) = 1 + 2\pi\rho \int_0^\infty r h(r) J_0(qr) dr, \tag{2}$$

where $h(r)$ is the total correlation function [16] and $J_0(qr)$ is a Bessel function of the first kind. Results from simulations at densities in the range $0.15 \leqslant \rho^* \leqslant 0.45$ are shown in Fig. 2. At low density ($\rho^* = 0.15$) $S(q)$ exhibits peaks at $q\sigma \simeq 2.6n$, with $n = 1, 2, 3, \ldots$, and is similar in form to that for a simple atomic fluid with particle diameter $2\pi\sigma/2.6 \simeq 2.4\sigma$ [16] (this distance being roughly equal to the average distance between nearest neighbors). Throughout the density range $0.25 \leqslant \rho^* \leqslant 0.45$ $S(q)$ exhibits peaks at $q\sigma \simeq 2.6$ and $q\sigma \simeq 5.5$. The features at $q\sigma \simeq 2.6$ still correspond to real-space separations in the region of $2\pi/q \simeq 2.4\sigma$, but these are now identified with the distances of closest approach between particles belonging to different clusters. The peak at $q\sigma \simeq 5.5$ corresponds to nearest-neighbor particles belonging to the same cluster, with a typical separation of $2\pi/q \simeq 1.1\sigma$.

A. Single-particle diffusion

It is well known that in simple low-density two-dimensional fluids, the velocity autocorrelation function, $C_v(t)$, possesses a characteristic t^{-1} long-time tail [20]. $C_v(t)$ is defined by

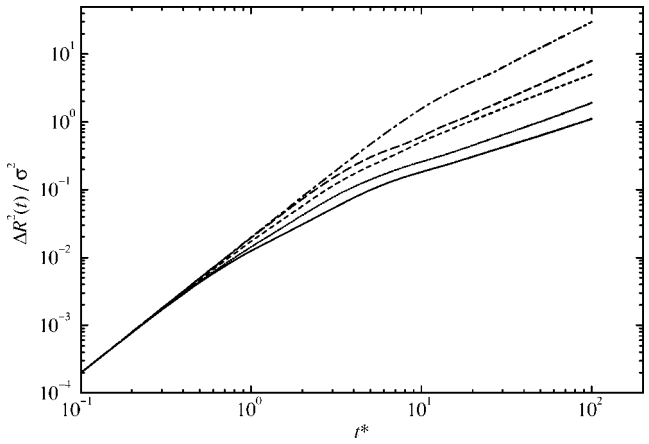

FIG. 3. Mean-squared displacement, $\Delta R^2(t)$, for systems at $T^*=0.01$ and densities $\rho^*=0.05$ (dot-dashed line), $\rho^*=0.15$ (long-dashed line), $\rho^*=0.25$ (dashed line), $\rho^*=0.35$ (dotted line), and $\rho^*=0.45$ (solid line).

$$C_v(t) = \left\langle \frac{1}{N}\sum_{j=1}^{N} \mathbf{v}_j(t)\cdot\mathbf{v}_j(0) \right\rangle, \tag{3}$$

where $\mathbf{v}_j(t)$ is the velocity of particle j at time t. If $C_v(t) \sim t^{-1}$ at long times, then the Green-Kubo relation for the diffusion constant, $D \propto \int_0^\infty C_v(t)$, diverges, implying that this transport coefficient is ill defined. This also implies that the mean-square displacement, $\Delta R^2(t)$, increases faster than t at long times, violating the Einstein relation $\lim_{t\to\infty}\Delta R^2(t) = 4Dt$. $\Delta R^2(t)$ is defined by

$$\Delta R^2(t) = \left\langle \frac{1}{N}\sum_{j=1}^{N} |\mathbf{r}_j(t) - \mathbf{r}_j(0)|^2 \right\rangle, \tag{4}$$

where $\mathbf{r}_j(t)$ is the position vector of particle j at time t. The long-time tail in $C_v(t)$ is attributed to hydrodynamic backflow effects [16], but it is wrong to assume that the long-time tail exists in *all* two-dimensional fluids. Notable exceptions include high-density soft-sphere fluids, in which $\Delta R^2(t)$ increases linearly with time over substantial time intervals [21–23]. Another example is the dipolar soft-sphere fluid at low concentrations and low temperature, where almost complete particle association appears to prevent hydrodynamic backflow [24].

The mean-square displacement, $\Delta R^2(t)$, in the CSF along the isotherm $T^*=0.01$ and at densities $\rho^*=0.05$, 0.15, 0.25, 0.35, and 0.45 is shown on a log-log plot in Fig. 3. At first glance, it appears that $\Delta R^2(t) \sim t$ at long times, which is characteristic of the diffusive regime. To examine this further, the time derivative of $\Delta R^2(t)$ is plotted in Fig. 4. If $\Delta R^2(t) \sim t$ at long times, then $\mathrm{d}\Delta R^2/\mathrm{d}t$ should tend toward a constant. Figure 4 demonstrates that this is not true for the lowest densities shown—$\rho^*=0.05$ and $\rho^*=0.15$—whereas the results for $\rho^* \geqslant 0.25$ appear to level off at long times. A close inspection of $\mathrm{d}\Delta R^2/\mathrm{d}t$ for all of the densities considered indicates that over the simulation time scale, the diffusion constant is well defined for densities at and above $\rho^*=0.25$, which coincides with the onset of extensive particle clustering (see Fig. 1).

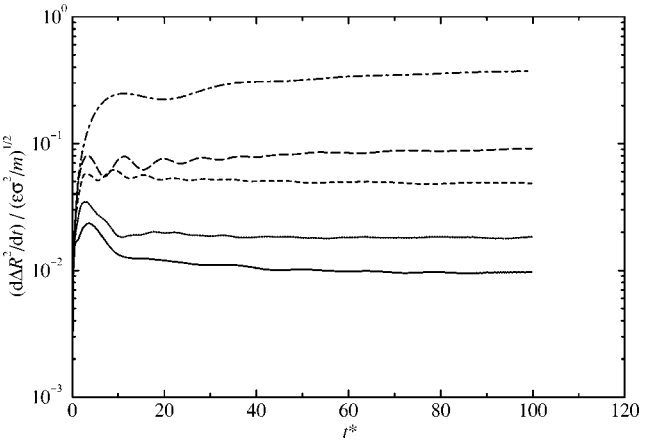

FIG. 4. Time derivative of the mean-squared displacement, $\mathrm{d}\Delta R^2(t)/\mathrm{d}t$, for systems at $T^*=0.01$ and densities $\rho^*=0.05$ (dot-dashed line), $\rho^*=0.15$ (long-dashed line), $\rho^*=0.25$ (dashed line), $\rho^*=0.35$ (dotted line), and $\rho^*=0.45$ (solid line). The results for $\rho^*=0.25$, 0.35, and 0.45 appear to level off at long times; estimates of the corresponding asymptotic values are indicated with faint lines.

This suggests that particle clustering mitigates against hydrodynamic effects (at least over the simulation time scale).

If the diffusion constant exists, then the Einstein relation implies that

$$D = \frac{1}{4}\lim_{t\to\infty}\frac{d\Delta R^2}{dt}. \tag{5}$$

For densities $\rho^* \geqslant 0.25$, the diffusion constant has been estimated using Eq. (5) with simulation results in the time interval $60 \leqslant t^* \leqslant 100$; the values are shown in Table I. Generally, the diffusion constant is expected to decrease with increasing density due to increasing confinement of the particles, although there appears to be a local maximum in the region of $\rho^*=0.37$. The chained structures at $\rho^* \simeq 0.35$ likely provide a strong hindrance to single-particle diffusion, but as the density is increased these chains must break up to form a network (as illustrated in Fig. 1). Therefore, it is possible that the increase in particle confinement with increasing density is overcompensated by the disintegration of the chains, lead-

TABLE I. Diffusion constant (D), shear viscosity (η), and high-frequency shear modulus (G_∞), in reduced units, for the CSF along the isotherm $T^*=0.01$ and at various densities, ρ^*.

ρ^*	$D\sqrt{m/\epsilon\sigma^2}$	$\eta\sqrt{\sigma^2/m\epsilon}$	$G_\infty\sigma^2/\epsilon$
0.25	$1.22(5)\times10^{-2}$	0.25	0.14
0.30	$1.10(2)\times10^{-2}$	0.26	0.25
0.31	$8.4(2)\times10^{-3}$	0.22	0.27
0.33	$5.4(2)\times10^{-3}$	0.81	0.32
0.35	$4.5(1)\times10^{-3}$	0.85	0.38
0.37	$5.9(1)\times10^{-3}$	0.61	0.46
0.39	$5.5(2)\times10^{-3}$	0.65	0.50
0.40	$4.7(2)\times10^{-3}$	0.88	0.53
0.45	$2.42(9)\times10^{-3}$	0.78	0.73

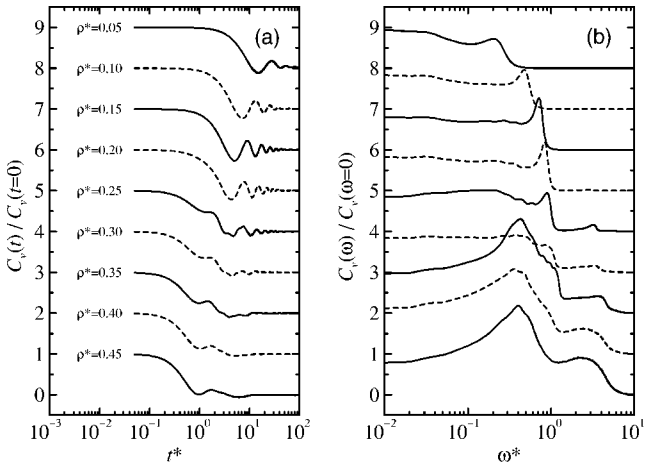

FIG. 5. Simulation results for (a) the velocity autocorrelation functions, $C_v(t)$, and (b) the associated Fourier transforms, $C_v(\omega)$, for the CSF along the isotherm $T^*=0.01$. In both (a) and (b) the curves are for systems with densities in the order, from top to bottom, $\rho^*=0.05$, 0.10, 0.15, 0.20, 0.25, 0.30, 0.35, 0.40, and 0.45. For clarity, the lines are drawn solid and dashed alternately, and are displaced from one another by one unit along the ordinate.

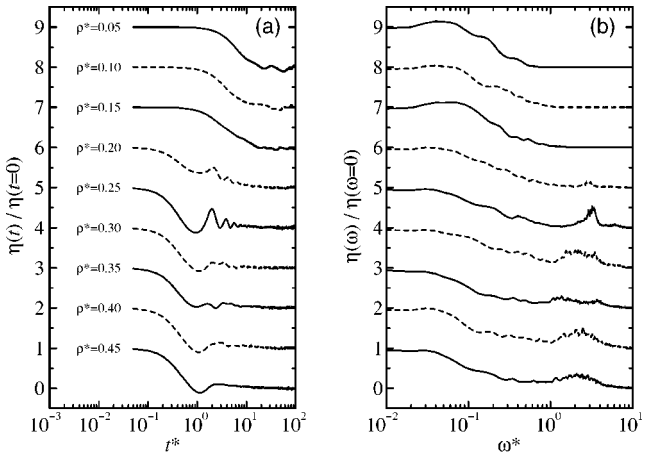

FIG. 6. Simulation results for (a) the shear-stress autocorrelation functions, $\eta(t)$, and (b) the associated Fourier transforms, $\eta(\omega)$, for the CSF along the isotherm $T^*=0.01$. In both (a) and (b) the curves are for systems with densities in the order, from top to bottom, $\rho^*=0.05$, 0.10, 0.15, 0.20, 0.25, 0.30, 0.35, 0.40, and 0.45. For clarity, the lines are drawn solid and dashed alternately, and are displaced from one another by one unit along the ordinate.

ing to a local maximum in D. At the highest densities—$\rho^*=0.40$ and 0.45—the effects of confinement are dominant.

To further investigate single-particle motions the velocity autocorrelation function $C_v(t)$ in (3) has been calculated. The spectrum of $C_v(t)$ will also be of interest:

$$C_v(\omega)=\int_{-\infty}^{\infty} C_v(t)\exp(-i\omega t)\mathrm{d}t. \tag{6}$$

$C_v(\omega)$ is only defined if $C_v(t)$ is integrable, but the results in Fig. 4 show that at low densities this is not the case since $C_v(t)$ must have a long-time tail. As a result, $C_v(t)$ has been Fourier transformed after application of a Blackman window [18]. Of course, at low densities this procedure will introduce an artificial low-frequency portion in $C_v(\omega)$, but it is assumed that the gross features of the spectrum will emerge unscathed. The normalized functions $C_v(t)/C_v(t=0)$ and $C_v(\omega)/C_v(\omega=0)$ for systems with densities in the range $0.05\leqslant\rho^*\leqslant0.45$ are presented in Fig. 5. At low densities ($\rho^*\leqslant0.20$) $C_v(t)$ shows damped oscillatory behavior characteristic of a dense atomic liquid. Although the particle density in the CSF is low, the effective diameter ($\sim2.4\sigma$)—and hence the "packing fraction"—at the low temperature considered will be large and so the oscillatory behavior is due to the backscattering processes familiar in dense atomic liquids [16]. $C_v(\omega)$ shows a clear peak at a frequency which increases with increasing density, reflecting the growing influence of backscattering. As the density is raised progressively above $\rho^*=0.20$ several new features in $C_v(\omega)$ emerge: a narrow band appears at high frequency ($\omega^*>1$); a broad band appears at low frequencies ($10^{-1}<\omega^*<1$); and the "backscattering" peak disappears under the emerging low-frequency band. With reference to Fig. 1, the density range $0.25\leqslant\rho^*\leqslant0.45$ is clearly identified with the development of particle clustering and so the high-frequency features likely arise from rapid single-particle motions within clusters, while the low-frequency band reflects some sort of coupling between single-particle motions and collective modes of the cluster network. These collective cluster motions (which are different from the hydrodynamic backflows responsible for long-time tails in low-density two-dimensional fluids) are examined further in Sec. III C.

B. Shear stress

The decay of shear-stress fluctuations was investigated using the shear-stress autocorrelation function,

$$\eta(t)=\frac{A}{k_BT}\langle\Pi_{xy}(t)\Pi_{xy}(0)\rangle, \tag{7}$$

in which $\Pi_{\alpha\beta}$ is an element of the stress tensor, given by,

$$\mathbf{\Pi}=\frac{1}{A}\left(\sum_{j=1}^{N}\frac{\mathbf{p}_j\mathbf{p}_j}{m}+\sum_{j=1}^{N}\sum_{k>j}^{N}\mathbf{r}_{jk}\mathbf{f}_{jk}\right), \tag{8}$$

where $\mathbf{p}_j$ is the momentum of particle j, $\mathbf{r}_{jk}$ is the separation vector between particles j and k, and $\mathbf{f}_{jk}$ is the force exerted on particle j by particle k. Simulation results for $\eta(t)/\eta(t=0)$ are shown in Fig. 6, along with the corresponding normalized Fourier transforms, $\eta(\omega)/\eta(\omega=0)$. As for the velocity autocorrelation functions, a Blackman window was applied to $\eta(t)$ prior to Fourier transformation. At low densities ($\rho^*\leqslant0.15$), $\eta(t)$ decays almost monotonically, with just a slight oscillation at long times (although this is within the noise). At higher densities ($\rho^*\geqslant0.20$) $\eta(t)$ exhibits a high-frequency modulation which is most pronounced at $\rho^*=0.25$, but then reduces to a dip at $\rho^*=0.45$. The dominant features in the spectra are broad low-frequency shoulders, and high-frequency bands that are present at densities $\rho^*\gtrsim0.20$. At $T^*=0.01$ the onset of particle clustering occurs in

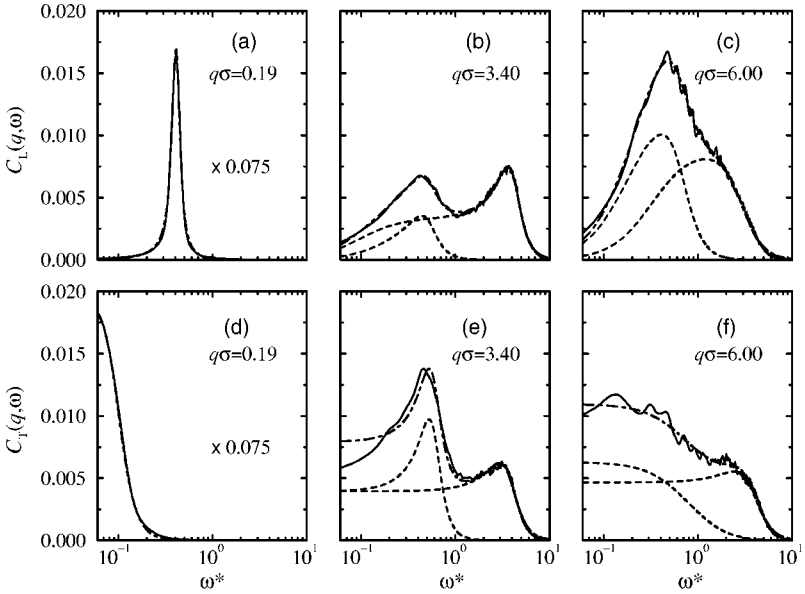

FIG. 7. $C_L(q,\omega)$ [(a)–(c)] and $C_T(q,\omega)$ [(d)–(f)] at the three different wave vectors indicated, for the CSF at $T^*=0.01$ and $\rho^*=0.45$: MD simulation results (solid lines); fits to simulation results using Eq. (14) for the longitudinal functions and Eq. (15) for the transverse functions (dot-dashed lines); and individual contributions from Eqs. (14) and (15) corresponding to $k=1$ and $k=2$ (dashed lines). The results at $q\sigma=0.19$ [(a) and (d)] have been scaled by a factor of 0.075 for clarity.

the vicinity of $\rho^*=0.20-0.25$ (see Ref. 13 and Fig. 1), and so the peaks in the region $\omega^*=1-2$ suggest some sort of local vibrational motion within clusters leading to the relaxation of shear-stress fluctuations.

The shear viscosity and high-frequency shear modulus were obtained from the Green-Kubo formula $\eta=\int_0^\infty \eta(t)\mathrm{d}t$ and the relation $G_\infty=\eta(0)$, respectively. Simulation results are presented in Table I. The high-frequency shear modulus is proportional to the average of Π_{xy}^2, and this is easy to calculate precisely in MD simulations. The shear viscosity, on the other hand, requires a precise calculation of $\eta(t)$, which can possess long-time or "molasses" tails. Therefore, Table I only reports values of η and G_∞ at densities $\rho^* \geqslant 0.25$. The shear viscosity jumps considerably between $\rho^*=0.31$ and $\rho^*=0.33$, presumably due to the development of chainlike ordering which persists over a considerable portion of the simulation cell. Over the density range $0.33 \leqslant \rho^* \leqslant 0.45$, η plateaus out at a roughly constant value [within the likely statistical errors of $\sim 10\%$ based on the noise in $\eta(t)$]. In this density range the cluster network percolates throughout the entire system. The high-frequency shear modulus increases monotonically with increasing density, reflecting the development of rigidity (over short time scales) as the cluster network is established.

C. Current correlation functions

To elucidate the nature of collective motions in the CSF, longitudinal (L) and transverse (T) modes have been examined through calculation of the corresponding current correlation functions,

$$C_\alpha(q,t)=\left\langle \frac{J_\alpha(\mathbf{q},t)J_\alpha(-\mathbf{q},0)}{N}\right\rangle, \tag{9}$$

where $\alpha=$L or T. The longitudinal and transverse currents are given by

$$J_L(\mathbf{q},t)=\frac{J_x(\mathbf{q},t)q_x+J_y(\mathbf{q},t)q_y}{q} \tag{10}$$

and

$$J_T(\mathbf{q},t)=\frac{-J_x(\mathbf{q},t)q_y+J_y(\mathbf{q},t)q_x}{q}, \tag{11}$$

respectively, where

$$\mathbf{J}(\mathbf{q},t)=\sum_{j=1}^{N}\mathbf{v}_j(t)\exp[-i\mathbf{q}\cdot\mathbf{r}_j(t)] \tag{12}$$

is a Fourier component of the current, and $\mathbf{q}=(q_x,q_y)$ is a wave vector commensurate with the periodic boundary conditions. Of more immediate use are the corresponding (temporal) Fourier transforms,

$$C_\alpha(q,\omega)=\int_{-\infty}^{\infty}C_\alpha(q,t)\exp(-i\omega t)\mathrm{d}t, \tag{13}$$

calculated after application of a windowing function to $C_\alpha(q,t)$ in case there are long-time tails (although in practice, no such features were detectable within the statistical noise). The CSF at a density $\rho^*=0.45$ and at temperature $T^*=0.01$ will be considered in detail, since at this state point the system exhibits a high degree of clustering and significant complexity in its intermediate-length-scale structure [see Fig. 1(e)]. The spectral functions $C_L(q,\omega)$ and $C_T(q,\omega)$ for this state point are shown in Fig. 7 at wave vectors $q\sigma=0.19$, 3.40, and 6.00. At the lowest wave vector ($q\sigma=0.19$) we find a single peak in $C_L(0.19\sigma^{-1},\omega)$ at finite frequency arising from an acoustic mode. $C_T(0.19\sigma^{-1},\omega)$ shows no finite-frequency maximum, as might be expected in the long-wavelength, hydrodynamic limit [15]. At an intermediate wave vector ($q\sigma=3.40$) both $C_L(3.40\sigma^{-1},\omega)$ and $C_T(3.40\sigma^{-1},\omega)$ show two maxima; in the transverse function these peaks correspond to propagating shear waves. At the highest wave vector ($q\sigma=6.00$) $C_L(6.00\sigma^{-1},\omega)$ and

$C_T(6.00\sigma^{-1},\omega)$ show pronounced shoulders on the high-frequency side of the main broad peak.

It is clear from Fig. 7 that at intermediate wave vectors there are two well-separated bands, perhaps corresponding to different types of motion. To analyze the relevant time scales in more detail, it is shown *a posteriori* that $C_\alpha(q,\omega)$ is well described using a simple superposition of functions—one for each band—taken from generalized hydrodynamics (see, e.g., Chap. 6 of Ref. [15]). In what follows, the effects of temperature fluctuations are ignored (i.e., the thermal conductivity $D_T=0$), and it is assumed that each channel for the relaxation of current correlations can be represented by a single exponential memory function. For the spectrum of the longitudinal current correlation function, the linear superposition is of the form [Eq. (6.3.36) of Ref. [15] with $D_T=0$]

$$C_L(q,\omega)=\sum_{k=1}^{2}\frac{a_k\omega\Phi'(\omega\tau_k)}{[\omega^2-\omega_k^2+b_k\Phi''(\omega\tau_k)]^2+[b_k\Phi'(\omega\tau_k)]^2}, \tag{14}$$

where $\Phi'(z)=z/(1+z^2)$ and $\Phi''(z)=-z^2/(1+z^2)$. For the transverse correlations [Eq. (6.2.25) of Ref. [15]],

$$C_T(q,\omega)=\sum_{k=1}^{2}\frac{a_k}{\left[\omega^2-\left(b_k-\frac{1}{2}\tau_k^{-2}\right)\right]^2+\left(b_k-\frac{1}{4}\tau_k^{-2}\right)\tau_k^{-2}}. \tag{15}$$

a_k, b_k, ω_k, and τ_k were treated as separate fitting parameters for each function and wave vector. It should be noted that the equations for $C_L(q,\omega)$ and $C_T(q,\omega)$ given in Ref. [15] involve combinations of q^2, k_BT, $S(q)$, etc., in place of the empirical parameters a_k, b_k, and ω_k given above. Factorization of these latter parameters is complicated by the question of how to apportion $S(q)$, etc. amongst the two contributions ($k=1$ and 2). In any case, the purpose of introducing Eqs. (14) and (15) is merely to aid fitting the simulation results. The resulting fits are included in Fig. 7, along with the individual contributions corresponding to the $k=1$ and $k=2$ terms in Eqs. (14) and (15). In the vicinities of the peaks the quality of the fits is excellent; the major deviations occur at very low frequencies (where the simulation results are less reliable anyway due to small truncation errors in the Fourier transforms) and at very high frequencies (where the generalized hydrodynamical description is expected to break down). Nonetheless, the simulation results are at least consistent with Eqs. (14) and (15), suggesting that there is a coexistence of distinct low- and high-frequency motions in the CSF.

The dispersions of the longitudinal and transverse modes in the CSF at $\rho^*=0.45$ and $T^*=0.01$ are shown in Fig. 8. These curves were constructed by plotting the peak frequencies, $\omega^*_{max}(q)$, from each of the $k=1$ and $k=2$ contributions to $C_\alpha(q,\omega)$ in Eqs. (14) and (15); the peak frequencies are listed in Table II. The high-frequency and low-frequency points are assigned to "primary" and "secondary" branches, respectively. The dispersion of longitudinal modes exhibits a primary branch similar in form to that of a simple fluid. The limiting slope of this branch as $q\to 0$ yields the speed of sound, c; from the points at $q\sigma\leqslant 1.79$, $c=(1.88\pm0.02)\sqrt{\epsilon/m}$. For iron particles (mass density 7.86 kg m^{-3}) of diameter 10 nm at a temperature $T=300$ K, this corresponds to $c=(600\pm10)$ m s^{-1}. At wave vectors $q\sigma\geqslant 2.62$, low-frequency peaks are observed in $C_L(q,\omega)$, the positions of which are plotted as the secondary branch in

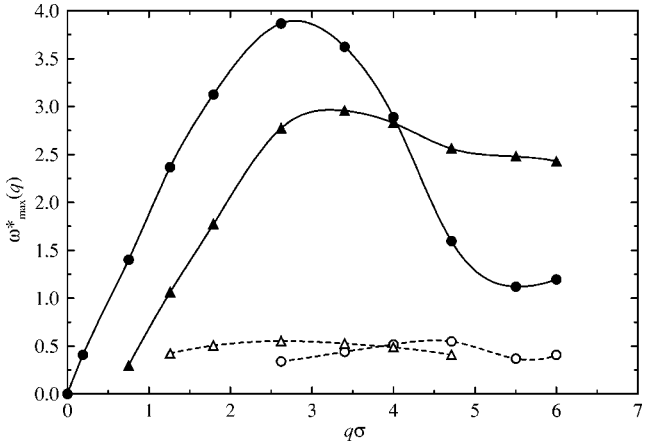

FIG. 8. Dispersion curves, $\omega^*_{max}(q)$, at $\rho^*=0.45$ and $T^*=0.01$ for longitudinal modes (circles) and transverse modes (triangles). The primary and secondary branches are indicated by filled and open symbols, respectively. The solid and dashed curves are Akima splines fitted to the primary and secondary branches, respectively.

TABLE II. Peak positions, $\omega^*_{max}(q)$, in the $k=1$ and $k=2$ contributions to $C_L(q,\omega)$ in (14) and $C_T(q,\omega)$ in (15) for the CSF at $T^*=0.01$ and at various densities. The peaks are grouped into a high-frequency "primary" branch, and a low-frequency "secondary" branch.

		Longitudinal		Transverse	
ρ^*	$q\sigma$	Primary branch	Secondary branch	Primary branch	Secondary branch
0.05	2.62		0.36		
0.10	2.62		0.37		
0.15	2.62		0.16		0.64
0.20	2.62		0.24	2.9 (weak)	0.74
0.25	2.62	3.1	0.21	3.1	0.51
0.30	2.62	3.4	0.16	2.8	0.52
0.35	2.62	4.1	0.42	1.9	0.51
0.40	2.62	3.8	0.23	2.6	0.54
0.45	0.19	0.41			
0.45	0.75	1.4		0.29	
0.45	1.26	2.4		1.1	0.42
0.45	1.79	3.1		1.8	0.51
0.45	2.62	3.9	0.34	2.8	0.55
0.45	3.40	3.6	0.44	3.0	0.53
0.45	4.00	2.9	0.52	2.8	0.49
0.45	4.71	1.6	0.55	2.6	0.41
0.45	5.50	1.1	0.37	2.5	
0.45	6.00	1.2	0.41	2.4	

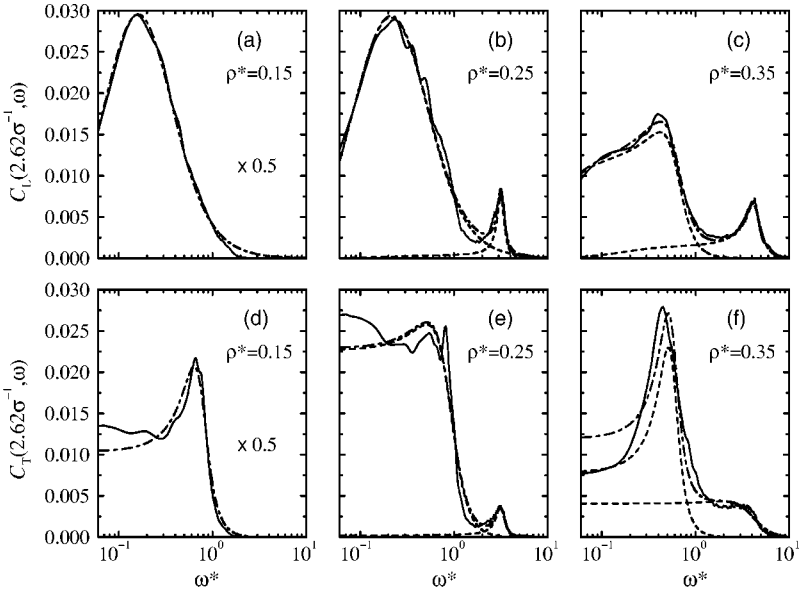

FIG. 9. $C_L(2.62\sigma^{-1},\omega)$ [(a)–(c)] and $C_T(2.62\sigma^{-1},\omega)$ [(d)–(f)] for the CSF at $T^*=0.01$, and at the densities indicated: MD simulation results (solid lines); fits to simulation results using Eq. (14) for the longitudinal functions and Eq. (15) for the transverse functions (dot-dashed lines); and individual contributions from Eqs. (14) and (15) corresponding to $k=1$ and $k=2$ (dashed lines). The results for $\rho^*=0.15$ [(a) and (d)] have been scaled by a factor of 0.5 for clarity.

Fig. 8. The peak in the primary branch and the appearance of the secondary branch occur at a wave vector $q\sigma\simeq 2.62$, which coincides with the position of the first peak in $S(q)$. At the state point considered, this wave vector corresponds to the typical size of the cavities in the meshlike structure. Dynamical modes corresponding to correlated motions of particles about "equilibrium" structures occur at low frequencies (and energies), and hence the low-frequency branch of the longitudinal dispersion is identified with such motions as "breathing" or other fluctuations in the shape and dimensions of the cavities. The primary branch shows a local minimum at $q\sigma\simeq 5.50$ which corresponds to the position of the second peak in $S(q)$. At the state point considered, this wave vector corresponds to the nearest-neighbor distance between particles in the same cluster. The high-frequency branch is therefore identified with "intracluster" motions involving neighboring particles bouncing off one another.

In a similar vein, the dispersion of transverse modes (shear waves) suggests a coexistence of low-frequency collective motions (observable at wave vectors $q\sigma\geqslant 1.26$) and high-frequency intracluster motions. The ringlike cavities shown in Fig. 1(e) are likely to support low-energy shearing motions, giving rise to the low-frequency branch. On the other hand, the high degree of local ordering within the fluid suggests an inherently rigid structure on short time scales, giving rise to a high-frequency branch.

Taken together, Figs. 2, 7, and 8 provide evidence for the bands in $C_\alpha(q,\omega)$ corresponding to low-frequency collective motions and high-frequency intracluster motions. The observation that $C_\alpha(q,\omega)$ can be accurately described by a simple superposition of two functions—as in Eqs. (14) and (15)—suggests that these motions are, to a first approximation, uncoupled.

For all densities in the range $0.25\leqslant\rho^*\leqslant 0.45$ the longitudinal and transverse dispersion curves appear to exhibit similar structures to those shown in Fig. 8. Like the structure factor, the form of the dispersion is relatively insensitive to variations in density within this range. As an illustration, the positions of the peaks in $C_\alpha(2.62\sigma^{-1},\omega)$ at different densities are collected in Table II. The fits to $C_L(2.62\sigma^{-1},\omega)$ and $C_T(2.62\sigma^{-1},\omega)$ for three sample densities ($\rho^*=0.15$, 0.25, and 0.35) are shown in Fig. 9. The variations of $\omega^*_{\max}(2.62\sigma^{-1})$ in the primary branches are not significant, while those in the secondary branches are more prominent. Even though the gross structures vary appreciably over the density range $0.25\leqslant\rho^*\leqslant 0.45$, they do share common motifs of clusters with near-neighbor separations $\simeq 1.1\sigma$, and mean separations between clusters $\simeq 2.4\sigma$. Hence, the assignments of low-frequency points to vibrations of the cluster network, and of high-frequency points to single-particle motions, are generally applicable to all densities at which significant clustering is apparent.

IV. CONCLUSIONS

Using molecular dynamics computer simulations, it has been shown how the structural complexity in a model one-component core-softened fluid is manifested in the single-particle and collective dynamics. All of the calculations reported in this work were for the model fluid at low temperature, and over a considerable range of density. At low densities, the fluid structure is quite simple, and the well-known long-time tail in the velocity autocorrelation function is clearly evident. The collective motions are also simple, there being only one characteristic time scale apparent in each current correlation function at a given wave vector.

At higher densities the fluid structure becomes considerably more complex, consisting of a wide variety of clustered motifs including (in order of increasing density) dimers, chains, and polygons. The mean-square displacement is seen to obey the Einstein relation, which suggests that the hydrodynamic backflow effects responsible for long-time tails in velocity autocorrelation functions are absent. The spectra of these latter functions show two distinct bands, which presumably reflect collective and single-particle motions. This situation is mirrored in the spectra of the shear-stress autocorrelation functions. The longitudinal and transverse current correlation functions clearly show the emergence of two dis-

tinct time scales accompanying the onset of particle clustering. Therefore, the longitudinal and transverse dispersion plots each possess two branches. By correlating the dispersion curves with the static structure factor, the high-frequency branches can be associated with the correlated motions of nearest neighbors within a given cluster, and the low-frequency branches with "breathing" or "shearing" motions of the underlying cluster network.

It is anticipated that similarly detailed simulation studies of three-dimensional core-softened fluids will yield further information on this interesting class of materials.

ACKNOWLEDGMENTS

I thank G. Malescio and G. Pellicane (Messina) for their interest in this work, and G. N. Patey (Vancouver) and A. J. Alexander (Edinburgh) for critical comments on an earlier version of this paper.

[1] P. H. Poole, F. Sciortino, U. Essmann, and H. E. Stanley, Nature (London) **360**, 324 (1992).
[2] Y. Katayama, T. Mizutani, W. Utsumi, O. Shimomura, M. Yamakata, and K. Funakoshi, Nature (London) **403**, 170 (2000).
[3] J. N. Glosli and F. H. Ree, Phys. Rev. Lett. **82**, 4659 (1999).
[4] E. A. Jagla, Phys. Rev. E **58**, 1478 (1998).
[5] E. A. Jagla, J. Chem. Phys. **111**, 8980 (1999).
[6] E. A. Jagla, Phys. Rev. E **63**, 061501 (2001).
[7] E. A. Jagla, Phys. Rev. E **63**, 061509 (2001).
[8] G. Malescio and G. Pellicane, Phys. Rev. E **63**, 020501(R) (2001).
[9] G. Malescio, G. Franzese, G. Pellicane, A. Skibinsky, S. V. Buldyrev, and H. E. Stanley, J. Phys.: Condens. Matter **14**, 2193 (2002).
[10] N. B. Wilding and J. E. Magee, Phys. Rev. E **66**, 031509 (2002).
[11] G. Franzese, G. Malescio, A. Skibinsky, S. V. Buldyrev, and H. E. Stanley, Phys. Rev. E **66**, 051206 (2002).
[12] G. Malescio and G. Pellicane, Nat. Mater. **2**, 97 (2003).
[13] P. J. Camp, Phys. Rev. E **68**, 061506 (2003).
[14] A. Skibinsky, S. V. Buldyrev, G. Franzese, G. Malescio, and H. E. Stanley, Phys. Rev. E **69**, 061206 (2004).
[15] J.-P. Boon and S. Yip, *Molecular Hydrodynamics* (Dover, New York, 1980).
[16] J.-P. Hansen and I. R. McDonald, *Theory of Simple Liquids* (Academic, London, 1986).
[17] J. Horbach, W. Kob, and K. Binder, Eur. Phys. J. B **19**, 531 (2001).
[18] M. P. Allen and D. J. Tildesley, *Computer Simulation of Liquids* (Clarendon, Oxford, 1987).
[19] T. A. Andrea, W. C. Swope, and H. C. Andersen, J. Chem. Phys. **79**, 4576 (1983).
[20] B. J. Alder and T. E. Wainwright, Phys. Rev. A **1**, 18 (1970).
[21] D. N. Perera and P. Harrowell, Phys. Rev. Lett. **80**, 4446 (1998).
[22] D. N. Perera and P. Harrowell, Phys. Rev. Lett. **81**, 120 (1998).
[23] D. N. Perera and P. Harrowell, J. Chem. Phys. **111**, 5441 (1999).
[24] P. D. Duncan and P. J. Camp, J. Chem. Phys. **121**, 11322 (2004).